NANO LETTERS
Letter
Cite This: Nano Lett. 2019, 19, 7301−7308
pubs.acs.org/NanoLett

Magnetic Proximity Coupling of Quantum Emitters in WSe_2 to van der Waals Ferromagnets

Kamran Shayan,[†,‡] Na Liu,[†,‡] Andrew Cupo,[§] Yichen Ma,[†,‡] Yue Luo,[†,‡] Vincent Meunier,[§] and Stefan Strauf*[,†,‡]

[†]Department of Physics, Stevens Institute of Technology, Hoboken, New Jersey 07030, United States
[‡]Center for Quantum Science and Engineering, Stevens Institute of Technology, Hoboken, New Jersey 07030, United States
[§]Department of Physics, Applied Physics, and Astronomy, Rensselaer Polytechnic Institute, Troy, New York 12180, United States

Supporting Information

ABSTRACT: The realization of on-chip quantum networks requires tunable quantum states to encode information carriers on them. We show that $Cr_2Ge_2Te_6$ (CGT) as a van der Waals ferromagnet can enable magnetic proximity coupling to site-controlled quantum emitters in WSe_2, giving rise to ultrahigh exciton g factors up to 20 ± 1. By comparing the same site-controlled quantum emitter before and after ferromagnetic proximity coupling, we also demonstrate a technique to directly measure the resulting magnetic exchange field (MEF) strength. Experimentally determined values of MEF up to 1.2 ± 0.2 meV in the saturation regime approach the theoretical limit of 2.1 meV that was determined from density functional theory calculations of the CGT/WSe_2 heterostructure. Our work extends the on-chip control of magneto-optical properties of excitons via van der Waals heterostructures to solid-state quantum emitters.

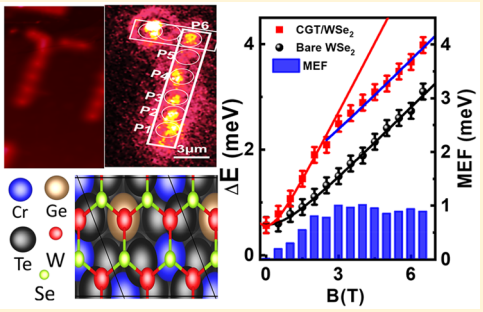

KEYWORDS: *2D materials, quantum emitter, van der Waals ferromagnet, magnetic proximity effect, g factor, magnetic exchange field*

Proximity effects have been known for decades to induce superconducting properties into adjacent normal metals on length scales approaching 100 μm.[1,2] In contrast, magnetic proximity effects, for example, from an adjacent ferromagnetic layer, decay over extremely short distances of a few nanometers and can typically be neglected in bulk materials. The field of van der Waals materials offers tremendous new opportunities to harness magnetic proximity effects due to their atomically thin nature. In general, the strong interaction can be generated by two effects:[3] On one hand, the wave function from the 2D material evanescently penetrates into an adjacent insulating ferromagnet, where it acquires exchange splitting from the native ferromagnet. On the other hand, the wave function of a metallic ferromagnet can directly polarize the electronic structure in the nonmagnetic 2D material. As a result, new ways are created to induce spin polarization, degeneracy-lifting, and symmetry-breaking effects. In this way, proximity-induced ferromagnetism was reported for metallic graphene and for topological insulators.[4,5]

Of much recent interest are semiconducting monolayers of transition-metal dichalcogenides (TMDCs) featuring strong spin−orbit coupling and intrinsic inversion symmetry breaking.[6,7] The valley degeneracy at K and K′ points in the conduction band can be lifted by an external magnetic field,[8,9] resulting in the moderate magnetic control of valley pseudospin splitting (∼0.1 meV/T) as well as optical addressing of K or K′ valleys using circularly polarized light,[10] giving rise to the upcoming field of valleytronics. The ability to further enhance the valley splitting energy of excitons in TMDCs is crucial to enable applications in on-chip quantum information processing, potentially even without an externally applied magnetic field. Ferromagnetic proximity coupling was recently demonstrated via polarized emission from the 2D neutral exciton in the conduction band, including WSe_2 attached to EuS,[11] WSe_2 attached to CrI_3,[12,13] and $MoTe_2$ on top of EuO.[14] Whereas large valley splitting energies up to ∼4 meV were achieved at modest external magnetic fields of 6 T[11] compared with the typical ∼1 meV at 6 T without proximity coupling, the effects nevertheless remain limited with respect to the rather broad spectral line width of several tens of millielectronvolts for the 2D exciton emission. Likewise, in $WSe_2/MoSe_2$ heterostructures, interlayer excitons form that feature giant effective g factors up to g = 15 and an energy splitting of 6 meV at 6 T, whereas spectra for both spin configurations still energetically overlap.[15]

To be relevant for encoding quantum information in the underlying spin states, the spin-polarized transitions need to be spectrally fully separated to avoid crosstalk in absorption/

Received: July 17, 2019
Revised: September 10, 2019
Published: September 24, 2019

DOI: 10.1021/acs.nanolett.9b02920
Nano Lett. 2019, 19, 7301−7308

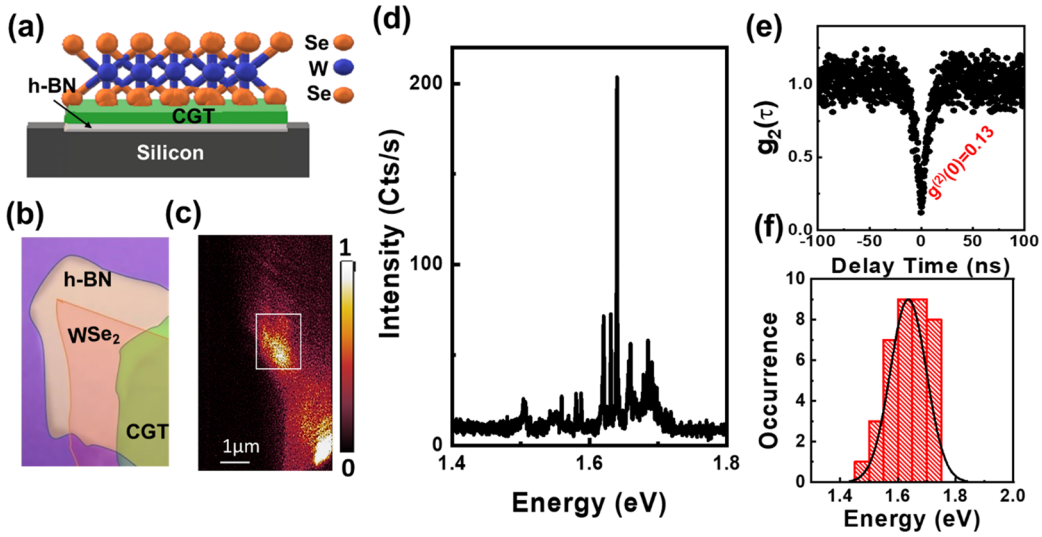

Figure 1. Optical characterization of quantum emitters in hBN/CGT/WSe_2 heterostructures. (a) Schematic of the layer stacking sequence. (b) Corresponding optical image (top view) of the heterostructure on SiO_2 substrate (purple). Colors and outlines are added to guide the eye. (c) Hyperspectral PL image filtered over the 750 nm band. The white box highlights a PL hot spot. (d) Exemplary PL spectra of the luminescence hot spot displaying sharp emission lines. (e) Second-order correlation function $g^2(0)$ of a spectrally filtered emission line under continuous-wave excitation showing pronounced photon antibunching with $g^{(2)}(0) = 0.13$. (f) Occurrence plot of quantum emitter emission energy distribution. All data were recorded at 4 K.

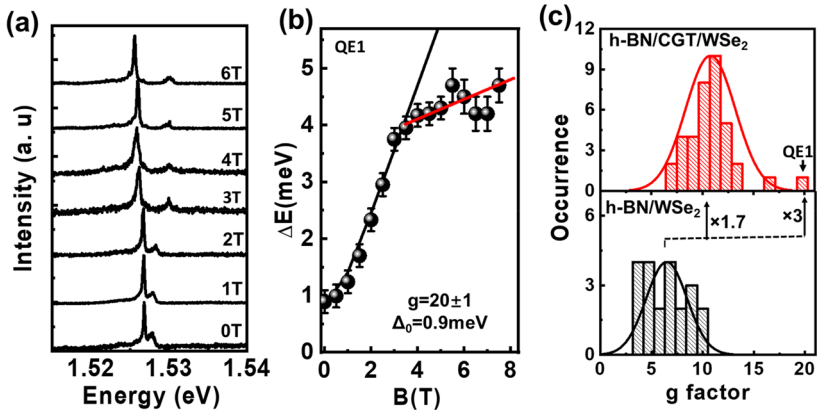

Figure 2. Magneto-optical characterization of a quantum emitter residing in the hBN/CGT/WSe_2 heterostructure region. (a) Magnetic dependence of exemplary photoluminescence spectra recorded in Faraday geometry. (b) Corresponding Zeeman energy splitting, ΔE, as a function of magnetic field strength, showing a g factor of $g = 20 \pm 1$ and a fine structure splitting $\Delta_0 = 0.95 \pm 0.05$ meV. The red solid line highlights the saturation behavior of the externally induced magnetization of the CGT layer. QE1: quantum emitter no. 1. (c) Corresponding occurrence histograms for exciton g factors recorded for the proximity-coupled quantum emitter in the hBN/CGT/WSe_2 region (top panel) and for the bare quantum emitter (hBN/WSe_2, bottom panel). The dashed line and arrow highlight the average (1.7-fold) and highest (3-fold) enhancement of the g factor. All data were recorded at 4 K.

emission, which was not yet achieved. Moreover, the emission from 2D excitons (neutral, charged, or interlayer) is limited to classical light emission and has no direct relevance to realizing spin-photon interfaces for quantum light states in the form of single or entangled photons. In contrast, 0D-like excitons in the TMDC monolayer emit single photons on demand and feature ultranarrow spectral line widths (<0.1 meV) with spectrally fully separated spin states.[16−19] These quantum emitters can also be externally induced via local stressors, randomly via nanobubbles,[20] along holes,[21] or spatially deterministic via dielectric or metallic pillars patterned onto a substrate,[22,23] and further deterministically coupled to plasmonic nanocavities.[24] Despite these appealing properties, the control and manipulation of quantum emitters via ferromagnetic proximity coupling has not yet been demonstrated.

Here we utilize the recently discovered van der Waals ferromagnetic crystals of $Cr_2Ge_2Te_6$ (CGT) that behaves in the thin layer form as an ideal Heisenberg ferromagnet below a Curie temperature of 60 K[25] and demonstrate pronounced proximity coupling to site-controlled quantum emitters in WSe_2. Magneto-optical measurements reveal a very large 0D exciton g factor up to $g = 20 \pm 1$ for heterostructures of monolayer WSe_2 and few-layer CGT, corresponding to a three-fold enhancement of the g factor compared with bare quantum emitters. By comparing the same quantum emitter before and after ferromagnetic proximity coupling, we also demonstrate a technique to directly measure the magnetic exchange field (MEF) strength, which approaches with experimental values

DOI: 10.1021/acs.nanolett.9b02920
Nano Lett. 2019, 19, 7301−7308

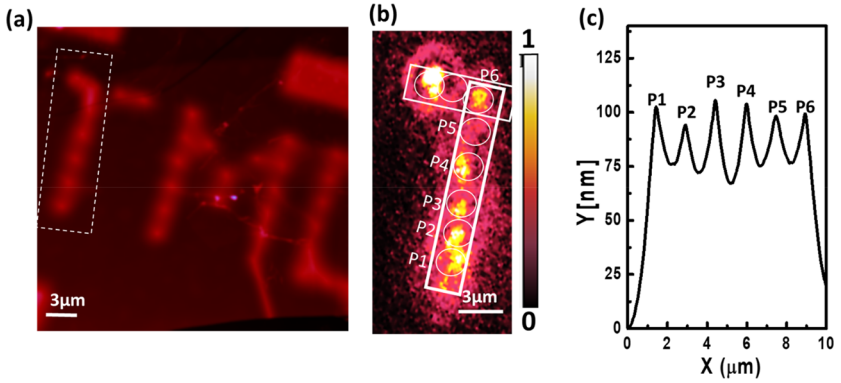

Figure 3. Optical characterization of WSe_2/CGT heterostructure stamped onto nanopillar arrays. (a) AFM image of WSe_2/CGT heterostructure over nanopillar arrays that trace out the letters TMDC (partial view). (b) Corresponding hyperspectral PL map for the 0D exciton emission in the 750 nm band recorded over the letter T. White circles highlight the correlations between nanopillars and PL hotspots. (C) Corresponding AFM line scanning across the long axis of the letter T from P1 to P6. AFM scans were carried out at room temperature, and the PL map was carried out at 4 K.

up to 1.2 meV the theoretical limit determined from density functional theory (DFT) calculations, revealing maximum values of 2.1 meV for the ideal van der Waals heterostructure.

Results. Because of the short-range nature of magnetic exchange coupling,[26,27] a high-quality and smooth interface between the van der Waals ferromagnet and the TMDCs[27] is a key requirement. Previously, we have shown that the encapsulation of monolayer TMDCs with thin films of hexagonal boron nitride (hBN) leads to a significant reduction of interface disorder, particularly from the Si/SiO_2 substrate, giving rise to an inhomogeneous exciton line width approaching the intrinsic limit.[28] In this work, we followed that approach and have passivated the silicon wafer by first exfoliating thin layers of hBN. Subsequent layers of CGT and WSe_2 have been transferred with thermal annealing between each step to avoid interface contamination. (See the Methods.). In this way, samples that feature both hBN/WSe_2 regions (uncoupled case) as well as heterostructures of hBN/CGT/WSe_2 (coupled case) have been created, as schematically depicted in Figure 1a, with a top view of the assembled heterostructure in Figure 1b. To deliberately create quantum emitters, we used cold stamping (room temperature) and hard pressing, an approach that we have previously shown to give rise to nanobubbles that create strain-induced 0D quantum emitters. (See the Methods.)[20] The corresponding 2D hyperspectral photoluminescence (PL) image of the hBN/CGT/WSe_2 heterostructure region highlights bright emission from a 0D quantum emitter (Figure 1c). Figure 1d displays an exemplary PL spectrum that feature a few sharp lines that are spectrally below the 2D exciton emission. When spectrally filtered, emission lines display pronounced single-photon emission signatures characterized by a second-order photon correlation function of $g^{(2)}(0) = 0.13$, as shown in Figure 1e. The energy range associated with these quantum emitters is shown in the occurrence plot in Figure 1f to vary in a rather well-defined energy range between 1.51 and 1.72 eV, depending on local strain.[22]

To investigate the magneto-PL properties of each quantum emitter, we applied the magnetic field parallel to the k vector of the incident laser (Faraday configuration). Figure 2a shows the magnetic field dependence of a quantum emitter with a fine structure splitting (FSS) at zero field Δ_0 of 900 μeV that originates from the electron−hole spin-exchange interaction as well as an underlying anisotropic strain, which also causes the low-energy peak of the doublet to dominate in the spectrum.[21] With increasing applied magnetic field, B, the two components of the clearly resolved Zeeman doublet split further apart. The Zeeman splitting energy, ΔE, was analyzed to determine the g factor using the well-known relation $\Delta E = \sqrt{\Delta_0^2 + (g\mu_0 B)^2}$, where μ_0 is the Bohr magneton and g is the exciton g factor. For the coupled case of a quantum emitter residing on the hBN/CGT/WSe_2 heterostructure, we determined an ultrahigh exciton g factor of $g = 20 \pm 1$, which is unprecedented in TMDC materials (Figure 2b). Interestingly, at magnetic field values above 3 T, the slope of the Zeeman splitting is drastically reduced, as indicated by the red solid line, corresponding to a much smaller g factor of 6.5 ± 0.5. This behavior is expected when the saturation magnetization of CGT has been reached ($3\mu_B$), above which any additional Zeeman splitting of the quantum emitter is driven by the increasing external magnetic field alone.

To provide statistical evidence as well as a reference for the g factor in the absence of CGT, we carried out magneto-PL measurements of 58 quantum emitters located on five different samples.

The statistical ensemble of 21 individual emitters residing on hBN/WSe_2 in the absence of ferromagnetic proximity coupling displays a large variety of g factors ranging from $g = 4.8$ to 9.8, with an average value from the occurrence plot of $g_{ave} = 6.4 \pm 2$ (Figure 2c, bottom). Note that the average value of the g factor for uncoupled emitter matches the finding of $g = 6.5$ in Figure 2b at higher fields, supporting the picture that CGT has reached full saturation under optical laser illumination at applied external fields around 3 T. The measured g factors for the uncoupled case are comparable to previous reports for 0D exciton g factors for quantum emitters in WSe_2,[16−22,29] which appear larger than g factors of 2D excitons and trions with typical values around $g = 4$.[30] It is found that about half of the quantum emitters display a nonmagnetic behavior, that is, a single peak with no zero-field splitting that does not split up even at high fields of 9 T.[29] Because no Zeeman effect is present in these cases, we naturally have excluded those from our study and only considered quantum emitters with magnetic behavior. In addition, we found that the g factor distribution for 0D quantum emitters in the uncoupled case weakly depends on the crystal growth technique when comparing samples grown by standard chemical vapor

DOI: 10.1021/acs.nanolett.9b02920
Nano Lett. 2019, 19, 7301−7308

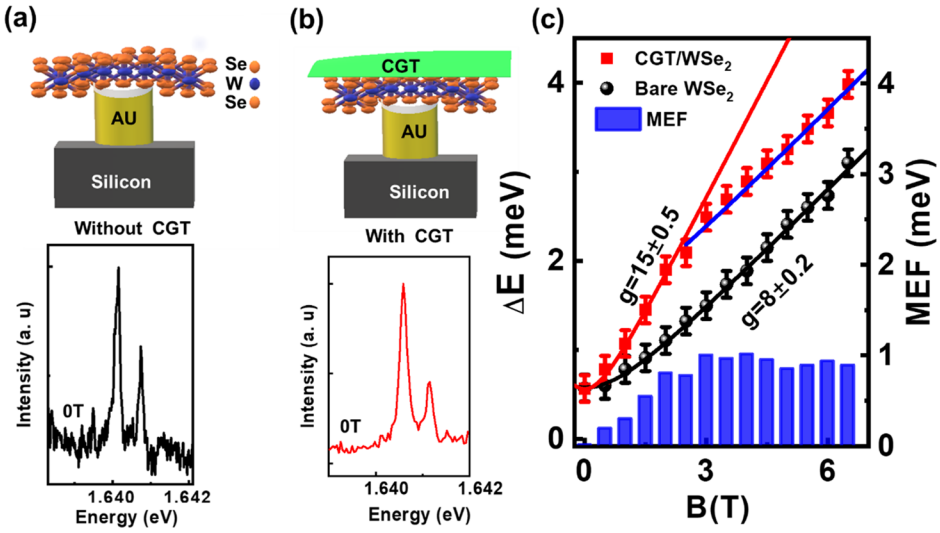

Figure 4. Magneto-optical characterization of quantum emitters in WSe_2/CGT heterostructures. (a) Schematic illustration of site-controlled quantum emitters in WSe_2 in their uncoupled state (top) and the corresponding magneto-PL spectrum recorded under 100 μW laser power and 1 s of integration time for the Zeeman doublet of an individual quantum emitter recorded at 0 T (bottom). (b) Same comparison as in panel a but after forming the heterostructure with CGT. Pump power was increased to 300 μW at 20 s of integration time to mitigate the absorption loss through CGT. Note that the Au nanopillars are capped by 2 nm Al_2O_3 to prevent PL quenching and spectral diffusion. (c) Zeeman splitting, ΔE, as a function of magnetic field before (black dots) and after proximity coupling (red dots). The red (black) solid lines are fits to the standard equation (see the text) to extract the g factor for the coupled (uncoupled) case with a value of $g = 15 \pm 0.5$ ($g = 8 \pm 0.2$). MEF: Magnetic exchange field, as determined from the energy difference of red and black data points at each magnetic field value. The blue solid line is a fit to the data above 3 T with a slope of $g = 8$, illustrating the saturation behavior of CGT. All data were recorded at 4 K.

transport (CVT) with the superior flux-growth technique that produces significantly higher quantum yield in the optical emission.[24,31] The latter displays slightly lower FSS and g factor values for the uncoupled case. (See Figure S1.)

Despite these large variations of the exciton g factor in the WSe_2 host crystal, Figure 2c (top) shows a clear difference for the 37 quantum emitters residing on hBN/CGT/WSe_2 that display g factor values under ferromagnetic proximity coupling varying from 7.2 to 20, with an average of $g_{ave} = 10.8 \pm 2.3$, which is 1.7 ± 0.3 times larger as compared with the average of the uncoupled case, whereas the best case ($g = 20$) is improved three-fold. The standard deviation of 0.3 corresponds to only a 17% variation, indicating that the g factors of all quantum emitters were enhanced by an underlying magnetic proximity coupling.

This demonstrated statistical approach is nevertheless limited because it is not possible to compare the same quantum emitter with and without proximity coupling. It thus remains unclear to what extent a change in microscopic origin from one quantum emitter to another or a change in local strain due to stamping onto CGT layers could cause a change in the 0D exciton g factor. To minimize variations from the growth process, we have solely utilized CVT-grown WSe_2 for the data set presented in the following. Previous work on quantum dots showed that the biaxial compressive strain of 0.025% induced via piezo actuators can lower the exciton g factor by ∼2%.[32] To exclude differences in microscopic origin as well as uncontrolled tensile strain as a cause of the observed proximity-enhanced g factor and to directly determine the MEF strength, we devised a measurement scheme to compare the same quantum emitter before and after coupling. To this end, we utilized the strain-induced quantum emitter formation via substrate nanopillars and further monitoring of the quantum emitter directly through the partially transparent CGT layer. Figure 3a shows an atomic force microscope (AFM) scan of the CGT/WSe_2 heterostructure stamped over a nanopillar array, which was patterned as the letters TMDC. (See the Methods.) After layer transfer, the 100 nm tall/wide nanopillars remain intact. The white box indicates the region for which the corresponding hyperspectral PL image filtered over the 1.7 meV energy range was recorded. The PL hotspots of the 0D exciton emission correlate nicely with the location of each nanopillar, as is evident from the hyperspectral mapping in Figure 3b. The corresponding AFM image in Figure 3c further indicates that only the nanopillars located at the outer edges provide a full strain modulation (100 nm), whereas the nanopillars located in between are modulated to only a ∼25 nm height difference at a separation of 1.5 μm. Nevertheless, this dense arrays of nanopillars produce a good yield, with six out of eight spatial sites inducing quantum emitters.

Quantum emitters induced by the stressors can be investigated for proximity coupling to CGT in two ways: (1) with CGT transferred first and WSe_2 on top or (2) the other way around. The former approach can maintain bright 0D exciton emission, giving rise to a proximity-enhanced g factor of $g = 11.2 \pm 0.2$ (Figure S2). Whereas this demonstrates the successful proximity coupling of spatially deterministic quantum emitters as compared with randomly located ones in Figure 2, the drawback of this approach is that, again, no information about the spectral properties of the emitter before attaching CGT can be recorded. In contrast, when first stamping WSe_2, the magneto-PL properties of the uncoupled case can be studied (Figure 4a) and directly compared with the case after transferring CGT on top (Figure 4b). In the latter case, the PL emission is significantly weaker due to the absorption loss through the CGT layer. To mitigate this effect, we increased the laser pump power from 100 to 300 μW and the integration time from 1 to 20 s to record PL spectra. The increased laser power causes a minor spectral broadening from 148 to 178 μeV from pump-induced exciton dephasing. As a

DOI: 10.1021/acs.nanolett.9b02920
Nano Lett. 2019, 19, 7301−7308

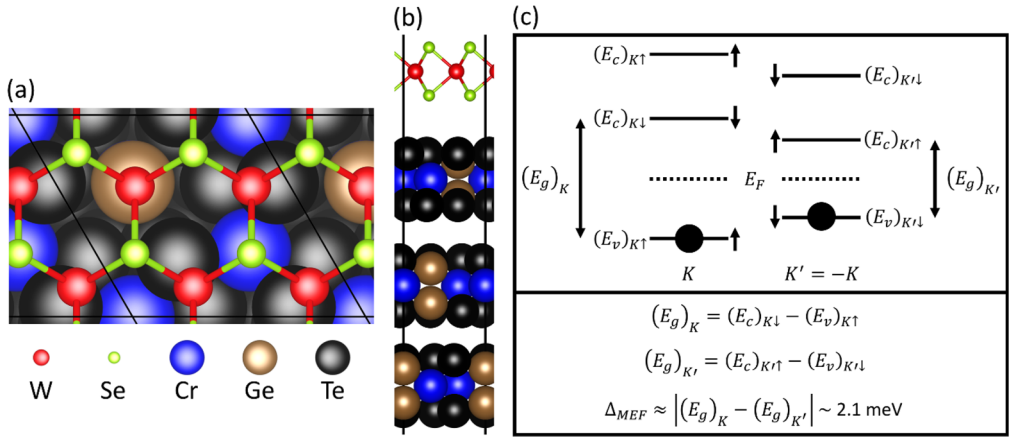

Figure 5. Atomic structure of WSe_2 on CGT optimized using density functional theory. (a) Top view. (b) Side view. (c) Energy level diagram illustrating the determination of the magnetic exchange field splitting, Δ_{MEF}. The level positions have been exaggerated for clarity.

key finding, the FSS at the zero field remains with $\Delta_0 = 570 \pm 15$ μeV before and $\Delta_0 = 560 \pm 15$ μeV after coupling unchanged, clearly indicating that the degree of strain anisotropy of the WSe_2 monolayer is not affected by the added material. In addition, a minor shift in the exciton emission of 1 meV to higher energies is most likely caused by a change in local strain after stamping of CGT. Following previous work on strain-tuning of quantum emitters,[21] a 1 meV change in energy corresponds to a relative strain variation of $\Delta\varepsilon = 0.02\%$ in the host crystal. Such a small change in local strain would cause only a minor change in the g factor of <2%, that is, an amount within the error bar of the determined g factors. Note that CGT is a soft ferromagnet[25] and thus displays only a small hysteresis effect in the electric resistivity below applied fields of 0.1 T.[33] The corresponding additional Zeeman energy for an exciton with a g factor of 10 and an applied magnetic field of 0.1 T is only 2 μeV, which is well below the exciton line width and is thus not resolvable.

The resulting ΔE values as a function of magnetic field are shown in Figure 4d. The solid lines follow $\Delta E = \sqrt{\Delta_0^2 + (g\mu_0 B)^2}$, resulting in $g = 8.0 \pm 0.2$ without and $g = 15 \pm 0.5$ with proximity coupling, corresponding to a 1.7-fold enhanced g factor, which is in close agreement with the average in ensemble studies (Figure 2). Above 3 T, the slopes of the Zeeman splitting for the uncoupled and coupled quantum emitter (solid blue trend line) are identical, clearly indicating that saturation magnetization of CGT has been reached. Because the same quantum emitter was measured with and without the ferromagnetic proximity layer, the additional Zeeman splitting by the underlying MEF can be directly determined from the energy difference between the two curves in Figure 4d, as shown by the blue bars. In this way, we determined an MEF value in the saturation regime of MEF = 1.05 ± 0.01 meV for this quantum emitter. In addition, Figure S3 and Figure S4 show two additional cases with comparable magnetic field behavior resulting in MEF = 1.2 ± 0.01 meV and MEF = 0.5 ± 0.01 meV, respectively. Given that the proximity effect varies exponentially with distance, we attribute the local variations in the experimentally determined interfacial MEF values to the observed surface roughness of 0.52 nm, as determined from AFM measurements of the heterostructure.

To determine an upper limit for MEF in the best case, that is, for an ideal heterostructure between WSe_2 and CGT without interface roughness, we have carried out theoretical modeling. It is expected that the g factor enhancement originates from the interfacial MEF, which is proportion to $\sim J\langle S_z\rangle$. In this framework, J is an exchange coupling between two adjacent atoms based on the Heisenberg model. At 4 K, and moderate external fields, $\langle S_z\rangle$ saturates at $3\mu_B$, as was experimentally determined for Cr^{3+} ions in CGT.[34] Previous efforts based on DFT calculation show that, depending on geometry, the nearest-neighbor intralayer J values and J interlayer exchange in the CGT lattice are in the range of −3.7 to 0.05 meV.[25] Because the proximity effects are strongly band-dependent,[35] we have carried out DFT calculations to gain insight into the mechanism for the enhancement of the effective exciton g factor in the adjacent WSe_2 monolayer based on the Perdew−Burke−Ernzerhof (PBE) functional. (See the Methods.) Top and side views of the optimized atomic model are shown in Figure 5a,b, respectively. We considered the ferromagnetic state of CGT with the magnetic moments of the Cr atoms pointing toward the WSe_2. The MEF splitting energy can be calculated from the electronic band structure from the K and K′ points in the first Brillouin zone, which is illustrated in Figure 5c. This model predicts a value of $\Delta_{MEF} = 2.1$ meV for our system. Note that for isolated WSe_2, the DFT calculated energy value is nearly three orders of magnitude smaller, which confirms that the predicted 2.1 meV splitting energy for the heterostructure is not influenced by numerical noise.

Apparently, the experimental values for MEF up to 1.2 meV approach the theoretical limit of 2.1 meV from the DFT calculations, indicating that the proximity coupling is only slightly degraded by interface roughness.

In summary, we have shown that magnetic proximity coupling of the van der Waals soft ferromagnet CGT with quantum emitters in WSe_2 gives rise to ultrahigh 0D exciton g factors up to $g = 20 \pm 1$. The observation of a clear saturation behavior of the CGT magnetization as well as the comparison of the same site-controlled quantum emitter before and after ferromagnetic proximity coupling allows us to directly quantify the interfacial magnetic change field via the additional induced Zeeman splitting. Our work extends the on-chip control of magneto-optical properties in van der Waals heterostructures previously reported for 2D excitons here to 0D excitons that are of interest to encode quantum information in the spin states of solid-state quantum emitters. In particular, if

DOI: 10.1021/acs.nanolett.9b02920
Nano Lett. 2019, 19, 7301−7308

combined with recent advances with hard ferromagnetic van der Waals materials such as Fe_3GeTe_2[36] as well as gate-controlled ferromagnetism,[37] the on-chip manipulation of magneto-optical properties of quantum emitters might become feasible, even in the absence of externally applied magnetic fields.

Methods. *Sample Preparation.* The CGT and hBN were mechanically exfoliated down to few-layer thin films (3−20 nm) from commercial crystals (HQ Graphene). Monolayers of WSe_2 were exfoliated either from commercial crystals (HQ Graphene) that were grown by CVT or from bulk crystals grown by the flux-growth technique that gives rise to one to two orders of magnitude lower defect density and higher exciton emission quantum yield, as we previously reported.[24,31] To achieve clean interfaces, we employed the "hot stamping" process[20] including substrate heating to 55 °C for the transfer process, followed by thermal annealing at 350 °C for 12 h between each stamping process. In contrast, to produce nanobubbles for the data in Figures 1 and 2, we utilized cold stamping: Samples were held at room temperature, stamping was carried out by hard pressing, and no additional thermal annealing was carried out in the last step to preserve the nanobubbles. To achieve spatially deterministic quantum emitter arrays, we fabricated Au nanopillar (100 nm tall and 100 nm diameter) arrays via electron-beam lithography (Elionix ELS-G100), followed by capping with 2 nm Al_2O_3 grown via atomic layer deposition, similar to our previous work on deterministic plasmonic coupling[24,31] but here on 90 nm SiO_2 substrates instead of sapphire and assembled into the letters "TMDC". The heterostructures were transferred onto the nanopillars by subsequent hot stamping to suppress detrimental nanobubble formation, either in CGT/WSe_2 or in WSe_2/CGT ordering configuration.

Photoluminescence Spectroscopy. Microphotoluminescence (μ-PL) measurements were taken inside a closed-cycle cryogen-free cryostat with a 3.8 K base temperature and ultralow vibration (attoDRY1100). Samples were excited with a laser diode operating at 532 nm in continuous-wave mode. A laser spot size of ∼0.85 μm was achieved using a cryogenic microscope objective lens with a numerical aperture of 0.82. The relative position between the sample and the laser spot was adjusted with a cryogenic piezoelectric xyz stepper, whereas 2D scan images were recorded with a cryogenic 2D-piezo scanner (Attocube). The spectral emission from the sample was collected in a multimode fiber, dispersed using a 0.75 m focal length spectrometer, and imaged by a liquid-nitrogen-cooled silicon charge-coupled device (CCD) camera.

Atomic Force Microscope Imaging. The AFM measurements were obtained using a Bruker Dimension FastScan AFM in noncontact mode at a scan rate of 1.3 Hz with a FastScan-B tip. The AFM high profiles were extracted from the images using Gwyddion open-source software.

Theoretical Methods. The plane-wave DFT calculations were carried out using VASP[38,39] with PAW pseudopotentials,[40] an energy cutoff of 500 eV, Gaussian smearing of 0.01 eV, the PBE exchange correlation functional,[41] gamma-centered k-point samplings, a force cutoff of 0.01 eV/Å for relaxations, and a vacuum spacing of ∼15 Å when appropriate. The lattice and ions were first optimized for single-layer WSe_2 (primitive cell, 16 × 16 × 1 k-point sampling) and bulk CGT (conventional standard cell with three layers per unit from Materials Project,[42] 8 × 8 × 3 k-point sampling). Even without using the PBE+U method, we found the correct ferromagnetic state for CGT, with ∼3μ_B per Cr atom. For the composite system, we considered the single layer of WSe_2 on three layers of CGT with the magnetic moment pointing toward the WSe_2. The lattice vectors of both materials are conveniently parallel, and to minimize the lattice mismatch, we used a (2 × 2) supercell of WSe_2 on a (1 × 1) cell of CGT. The in-plane lattice vectors of the CGT were compressed by 4% to exactly match those of the isolated WSe_2 supercell, which is similar to what was required when WSe_2 on ferromagnetic EuS was studied.[11] Straining the substrate instead of the adsorbate prevents a band alignment modification for the system component of interest.[43] The bulk CGT ions were first relaxed with the new lattice constant imposed, and the local magnetic moments changed by only ∼0.1μ_B per Cr atom as compared with the unstrained bulk. To form the final composite system, the ions were relaxed, keeping the two bottom layers of the CGT fixed to simulate a "bulk" substrate (8 × 8 × 1 k-point sampling). Spin−orbit coupling was included throughout all calculations. Site projections were used to determine the bands belonging to WSe_2 near the Fermi energy.

■ ASSOCIATED CONTENT

Supporting Information

The Supporting Information is available free of charge on the ACS Publications website at DOI: 10.1021/acs.nanolett.9b02920.

(1) Magneto-PL properties of quantum emitters in the flux-grown versus CVT-grown crystals of WSe_2, (2) site-controlled quantum emitters in CGT/WSe_2 heterostructures, (3) site-controlled quantum emitters in WSe_2/CGT heterostructures (PDF)

■ AUTHOR INFORMATION

Corresponding Author

*E-mail: strauf@stevens.edu.

ORCID

Yue Luo: 0000-0002-2757-5395

Vincent Meunier: 0000-0002-7013-179X

Stefan Strauf: 0000-0002-9887-7059

Notes

The authors declare no competing financial interest.

■ ACKNOWLEDGMENTS

We thank Bumhu Kim, Katayun Barmak, and James C. Hone at Columbia University for providing us with flux-grown WSe_2 crystals for the comparison in Figure S1. S.S. acknowledges financial support by the National Science Foundation (NSF) under awards DMR-1809235 and ECCS-MRI-1531237. A.C. was supported by NSF grant EFRI 2-DARE (EFRI-1542707) and by a DOE SCGSR award. This material is based upon work supported by the U.S. Department of Energy, Office of Science, Office of Workforce Development for Teachers and Scientists, Office of Science Graduate Student Research (SCGSR) program. The SCGSR program is administered by the Oak Ridge Institute for Science and Education (ORISE) for the DOE. ORISE is managed by ORAU under contract number DE-SC0014664. All opinions expressed in this paper are the authors' and do not necessarily reflect the policies and views of DOE, ORAU, or ORISE.

DOI: 10.1021/acs.nanolett.9b02920
Nano Lett. 2019, 19, 7301−7308

REFERENCES

(1) Wolf, E. L. Electron Tunneling Spectroscopy. *Rep. Prog. Phys.* **1978**, *41*, 1439.
(2) Kompaniiets, M.; Dobrovolskiy, O. V.; Neetzel, C.; Ensinger, W.; Huth, M. Superconducting Proximity Effect in Crystalline Co and Cu Nanowires. *J. Supercond. Novel Magn.* **2015**, *28*, 431.
(3) Lazić, P.; Belashchenko, K. D.; Žutić, I. Effective Gating and Tunable Magnetic Proximity Effects in Two-dimensional Heterostructures. *Phys. Rev. B: Condens. Matter Mater. Phys.* **2016**, *93*, 241401.
(4) Wang, Z.; Tang, C.; Sachs, R.; Barlas, Y.; Shi, J. Proximity-Induced Ferromagnetism in Graphene Revealed by the Anomalous Hall Effect. *Phys. Rev. Lett.* **2015**, *114*, 016603.
(5) Katmis, F.; Lauter, V.; Nogueira, F. S.; Assaf, B. A.; Jamer, M. E.; Wei, P.; Satpati, B.; Freeland, J. W.; Eremin, I.; Heiman, D.; Jarillo-Herrero, P. A.; Moodera, J. S. High-Temperature Ferromagnetic Topological Insulating Phase by Proximity Coupling. *Nature* **2016**, *533*, 513−516.
(6) Xiao, D.; Liu, G.-B.; Feng, W.; Xu, X.; Yao, W. Coupled Spin and Valley Physics in Monolayers of MoS_2 and other Group-VI Dichalcogenides. *Phys. Rev. Lett.* **2012**, *108*, 196802.
(7) Zhu, Z. Y.; Cheng, Y. C.; Schwingenschlögl, U. Giant Spin-Orbit-Induced Spin Splitting in Two-Dimensional Transition Metal Dichalcogenide Semiconductors. *Phys. Rev. B: Condens. Matter Mater. Phys.* **2011**, *84*, 153402.
(8) Aivazian, G.; Gong, Z.; Jones, A. M.; Chu, R. L.; Yan, J.; Mandrus, D. G.; Zhang, C.; Cobden, D.; Yao, W.; Xu, X. Magnetic Control of Valley Pseudospin in Monolayer WSe_2. *Nat. Phys.* **2015**, *11*, 148−152.
(9) MacNeill, D.; Heikes, C.; Mak, K. F.; Anderson, Z.; Kormányos, A.; Zólyomi, V.; Park, J.; Ralph, D. C. Breaking of Valley Degeneracy by Magnetic Field in Monolayer $MoSe_2$. *Phys. Rev. Lett.* **2015**, *114*, 037401.
(10) Cao, T.; Wang, G.; Han, W.; Ye, H.; Zhu, C.; Shi, J.; Niu, Q.; Tan, P.; Wang, E.; Liu, B.; Feng, J. Valley-Selective Circular Dichroism of Monolayer Molybdenum Disulphide. *Nat. Commun.* **2012**, *3*, 887.
(11) Zhao, C.; Norden, T.; Zhang, P.; Zhao, P.; Cheng, Y.; Sun, F.; Parry, J. P.; Taheri, P.; Wang, J.; Yang, Y.; Scrace, T.; Kang, K.; Yang, S.; Miao, G.; Sabirianov, R.; Kioseoglou, G.; Huang, W.; Petrou, A.; Zeng, H. Enhanced Valley Splitting in Monolayer WSe_2 due to Magnetic Exchange Field. *Nat. Nanotechnol.* **2017**, *12*, 757−762.
(12) Zhong, D.; Seyler, K. L.; Linpeng, X.; Cheng, R.; Sivadas, N.; Huang, B.; Schmidgall, E.; Taniguchi, T.; Watanabe, K.; McGuire, M. A.; et al. Van der Waals Engineering of Ferromagnetic Semiconductor Heterostructures for Spin and Valleytronics. *Sci. Adv.* **2017**, *3*, e1603113.
(13) Seyler, K.; Zhong, D.; Huang, B.; Linpeng, X.; Wilson, N. P.; Taniguchi, T.; Watanabe, K.; Yao, W.; Xiao, D.; McGuire, M. A.; et al. Valley Manipulation by Optically Tuning the Magnetic Proximity Effect in WSe_2/CrI_3 Heterostructures. *Nano Lett.* **2018**, *18*, 3823−3828.
(14) Zhang, Q.; Yang, S. A.; Mi, W.; Cheng, Y.; Schwingenschlögl, U. Large Spin-Valley Polarization in Monolayer $MoTe_2$ on Top of EuO (111). *Adv. Mater.* **2016**, *28*, 959−966.
(15) Nagler, P.; Ballottin, M. V.; Mitioglu, A.; Mooshammer, F.; Paradiso, N.; Strunk, C.; Huber, R.; Chernikov, A.; Christianen, P. C.; Schüller, C.; Korn, T. Giant Magnetic Splitting Inducing Near-Unity Valley Polarization in Van Der Waals Heterostructures. *Nat. Commun.* **2017**, *8*, 1551.
(16) Srivastava, A.; Sidler, M.; Allain, A. V.; Lembke, D. S.; Kis, A.; Imamoglu, A. Optically Active Quantum Dots in Monolayer WSe_2. *Nat. Nanotechnol.* **2015**, *10*, 491−496.
(17) Chakraborty, C.; Kinnischtzke, L.; Goodfellow, K. M.; Beams, R.; Vamivakas, A. N. Voltage-Controlled Quantum Light from an Atomically Thin Semiconductor. *Nat. Nanotechnol.* **2015**, *10*, 507−511.
(18) He, Y. M.; Clark, G.; Schaibley, J. R.; He, Y.; Chen, M. C.; Wei, Y. J.; Ding, X.; Zhang, Q.; Yao, W.; Xu, X.; Lu, C. Y.; Pan, J. W. Single Quantum Emitters in Monolayer Semiconductors. *Nat. Nanotechnol.* **2015**, *10*, 497−502.
(19) Koperski, M.; Nogajewski, K.; Arora, A.; Cherkez, V.; Mallet, P.; Veuillen, J. Y.; Marcus, J.; Kossacki, P.; Potemski, M. Single Photon Emitters in Exfoliated WSe_2 Structures. *Nat. Nanotechnol.* **2015**, *10*, 503−506.
(20) Shepard, G. D.; Ajayi, O. A.; Li, X.; Zhu, X. Y.; Hone, J. C.; Strauf, S. Nanobubble Induced Formation of Quantum Emitters in Monolayer Semiconductors. *2D Mater.* **2017**, *4*, 021019.
(21) Kumar, S.; Kaczmarczyk, A.; Gerardot, B. D. Strain-Induced Spatial and Spectral Isolation of Quantum Emitters in Mono-and Bilayer WSe_2. *Nano Lett.* **2015**, *15*, 7567−7573.
(22) Branny, A.; Kumar, S.; Proux, R.; Gerardot, B. D. Deterministic Strain-Induced Arrays of Quantum Emitters in a Two-Dimensional Semiconductor. *Nat. Commun.* **2017**, *8*, 15053.
(23) Palacios-Berraquero, C.; Kara, D. M.; Montblanch, A. R. P.; Barbone, M.; Latawiec, P.; Yoon, D.; Ott, A. K.; Loncar, M.; Ferrari, A. C.; Atatüre, M. Large-Scale Quantum-Emitter Arrays in Atomically Thin Semiconductors. *Nat. Commun.* **2017**, *8*, 15093.
(24) Luo, Y.; Shepard, G. D.; Ardelean, J. V.; Rhodes, D. A.; Kim, B.; Barmak, K.; Hone, J. C.; Strauf, S. Deterministic Coupling of Site-Controlled Quantum Emitters in Monolayer WSe_2 to Plasmonic Nanocavities. *Nat. Nanotechnol.* **2018**, *13*, 1137−1142.
(25) Gong, C.; Li, L.; Li, Z.; Ji, H.; Stern, A.; Xia, Y.; Cao, T.; Bao, W.; Wang, C.; Wang, Y.; et al. Discovery of Intrinsic Ferromagnetism in Two-Dimensional van der Waals Crystals. *Nature* **2017**, *546*, 265−269.
(26) Scharf, B.; Xu, G.; Matos-Abiague, A.; Žutić, I. Magnetic Proximity Effects in Transition-Metal Dichalcogenides: Converting Excitons. *Phys. Rev. Lett.* **2017**, *119*, 127403.
(27) Žutić, I.; Matos-Abiague, A.; Scharf, B.; Dery, H.; Belashchenko, K. Proximitized Materials. *Mater. Today* **2019**, *22*, 85−107.
(28) Ajayi, O. A.; Ardelean, J. V.; Shepard, G. D.; Wang, J.; Antony, A.; Taniguchi, T.; Watanabe, K.; Heinz, T. F.; Strauf, S.; Zhu, X.-Y.; Hone, J. C. Approaching the Intrinsic Photoluminescence Linewidth in Transition Metal Dichalcogenide Monolayers. *2D Mater.* **2017**, *4*, 031011.
(29) Kumar, S.; Brotóns-Gisbert, M.; Al-Khuzheyri, R.; Branny, A.; Ballesteros-Garcia, G.; Sánchez-Royo, J. F.; Gerardot, B. D. Resonant Laser Spectroscopy of Localized Excitons in Monolayer WSe_2. *Optica* **2016**, *3*, 882−886.
(30) Srivastava, A.; Sidler, M.; Allain, A. V.; Lembke, D. S.; Kis, A.; Imamoglu, A. Valley Zeeman Effect in Elementary Optical Excitations of Monolayer WSe_2. *Nat. Phys.* **2015**, *11*, 141−147.
(31) Luo, Y.; Liu, N.; Li, X.; Hone, J. C.; Strauf, S. Single Photon Emission in WSe_2 Up 160 K by Quantum Yield Control. *2D Mater.* **2019**, *6*, 035017.
(32) Tholen, H. M. G. A.; Wildmann, J. S.; Rastelli, A.; Trotta, R.; Pryor, C. E.; Zallo, E.; Schmidt, O. G.; Koenraad, P. M.; Silov, A. Y. Strain-Induced *g*-Factor Tuning in Single InGaAs/GaAs Quantum Dots. *Phys. Rev. B: Condens. Matter Mater. Phys.* **2016**, *94*, 245301.
(33) Lohmann, M.; Su, T.; Niu, B.; Hou, Y. S.; Alghamdi, M.; Aldosary, M.; Xing, W.; Zhong, J.; Jia, S.; Han, W.; et al. Probing Magnetism in Insulating $Cr_2Ge_2Te_6$ by Induced Anomalous Hall Effect in Pt. *Nano Lett.* **2019**, *19*, 2397−2403.
(34) Carteaux, V.; Brunet, D.; Ouvrard, G.; Andre, G. Crystallographic Magnetic and Electronic Structures of a New Layered Ferromagnetic Compound $Cr_2Ge_2Te_6$. *J. Phys.: Condens. Matter* **1995**, *7*, 69.
(35) Zollner, K.; Gmitra, M.; Fabian, F. Electrically Tunable Exchange Splitting in Bilayer Graphene on Monolayer $Cr_2X_2Te_6$ with X = Ge, Si, and Sn. *New J. Phys.* **2018**, *20*, 073007.
(36) Fei, Z.; Huang, B.; Malinowski, P.; Wang, W.; Song, T.; Sanchez, J.; Yao, W.; Xiao, D.; Zhu, X.; May, A. F.; Wu, W.; Cobden, D. H.; Chu, J. H.; Xu, X. Two-Dimensional Itinerant Ferromagnetism in Atomically Thin Fe_3GeTe_2. *Nat. Mater.* **2018**, *17*, 778.
(37) Deng, Y.; Yu, Y.; Song, Y.; Zhang, J.; Wang, N. Z.; Sun, Z.; Yi, Y.; Wu, Y. Z.; Wu, S.; Zhu, J.; Wang, J.; Chen, X. H.; Zhang, Y. Gate-

DOI: 10.1021/acs.nanolett.9b02920
Nano Lett. 2019, 19, 7301−7308

Tunable Room-Temperature Ferromagnetism in Two-Dimensional Fe_3GeTe_2. *Nature* **2018**, *563*, 94−99.
(38) Kresse, G.; Furthmüller, J. Efficiency of ab-initio Total Energy Calculations for Metals and Semiconductors Using a Plane-Wave Basis Set. *Comput. Mater. Sci.* **1996**, *6*, 15−50.
(39) Kresse, G.; Furthmüller, J. Efficient Iterative Schemes For ab Initio Total Energy Calculations Using a Plane-Wave Basis Set. *Phys. Rev. B: Condens. Matter Mater. Phys.* **1996**, *54*, 11169.
(40) Blöchl, P. E. Projector Augmented-Wave Method. *Phys. Rev. B: Condens. Matter Mater. Phys.* **1994**, *50*, 17953.
(41) Perdew, J. P.; Burke, K.; Ernzerhof, M. Generalized Gradient Approximation Made Simple. *Phys. Rev. Lett.* **1996**, *77*, 3865.
(42) Jain, A.; Ong, S. P.; Hautier, G.; Chen, W.; Richards, W. D.; Dacek, S.; Cholia, S.; Gunter, D.; Skinner, D.; Ceder, G.; Persson, K. A. Commentary: The Materials Project: A Materials Genome Approach to Accelerating Materials Innovation. *APL Mater.* **2013**, *1*, 011002.
(43) Johari, P.; Shenoy, V. B. Tuning the Electronic Properties of Semiconducting Transition Metal Dichalcogenides by Applying Mechanical Strains. *ACS Nano* **2012**, *6*, 5449−5456.

DOI: 10.1021/acs.nanolett.9b02920
Nano Lett. 2019, 19, 7301−7308